MDPI

Article

Prediction of Pore Volume Dispersion and Microstructural Characteristics of Concrete Using Image Processing Technique

Dhanalakshmi K [1], Maheswaran. J [2], Siva Avudaiappan [3,*], Mugahed Amran [4,5,*], Radhamanohar Aepuru [6], Roman Fediuk [7] and Nikolai Vatin [8]

[1] Department of Civil Engineering, University College of Engineering, Nagercoil 629004, TN, India; dhanu_krisha@yahoo.co.in
[2] Department of Civil Engineering, St. Xaviers Catholic College of Engineering, Nagercoil 629004, TN, India; jmaheswaran61@gmail.com
[3] Departamento de Ingeniería en Obras Civiles, Universidad de Santiago de Chile, Av. Ecuador 3659, Estación Central, Santiago 9160000, Chile
[4] Department of Civil Engineering, College of Engineering, Prince Sattam Bin Abdulaziz University, Alkharj 16273, Saudi Arabia
[5] Department of Civil Engineering, Faculty of Engineering and IT, Amran University, Amran 9677, Yemen
[6] Departamento de Ingeniería Mecánica, Facultad de Ingeniería, Universidad Tecnologica Metropolitana, Santiago 8330378, Chile; raepuru@utem.cl
[7] Polytechnic Institute, Far Eastern Federal University, 690922 Vladivostok, Russia; fedyuk.rs@dvfu.ru
[8] Peter the Great St. Petersburg Polytechnic University, 195251 St. Petersburg, Russia; vatin@mail.ru
* Correspondence: siva.avudaiappan@usach.cl (S.A.); m.amran@psau.edu.sa (M.A.)

Abstract: Concrete has served an essential role in many infrastructural projects. Factors including pore percentage, pore distribution, and cracking affect concrete durability. This research aims to better understand pore size distribution in cement-based materials. Micro-computed tomography (micro-CT) pictures were utilised to characterise the interior structure of specimens without destroying them. The pore dispersion of the specimens was displayed in 3D, utilising the data and imaging techniques collected, and the pore volume dispersion was examined using a volume-based approach. Another way to describe heterogeneous pore features is the chord-length distribution, which was calculated from three-dimensional micro-CT scans and correlated with the traditional method. The collected specimens were subjected to physical and mechanical testing. In addition, image processing techniques were used to conduct the studies. The results showed that the chord-length distribution-based pore size distribution is very successful than the traditional volume-based technique. The acquired data could be used for research and to forecast the characteristics of the materials.

Keywords: image processing; pore microstructure; multiphysics concrete model; SEM

1. Introduction

Concrete is one of the most extensively utilised building materials in the world. Aggregates, cement, water, and any other additives required to achieve the specified specification of concrete. C_2S, C_3A, C_3S, C_4AF, and CSH_2 are the five major components of cement which determines the strength of concrete. In concrete, porosity is one of the important characteristics that directly affects the strength and durability of cement-based materials [1,2]. Gel pores, capillary pores, and air Voids make up the pore structure of cement-based materials, and the pores are randomly sized, organised, and connected [3]. Two- and three-dimensional (2D and 3D) imaging methods were used to compare the pore volume dispersion of concrete with varied air entraining admixture doses to anticipate the material characteristics. The relationship between the pore features of the specimens and their mechanical properties was investigated. As concrete buildings are subjected to a variety of hazardous conditions, research into the long-term durability of cementitious composites has attracted much interest. Concrete is prone to degradation during freeze/thaw cycles [4],

and as a result, it can degrade visibly in the winter. The hazard of concrete degradation due to freeze-thaw cycles is significant in critical applications, including foundations, dams, pavements, and bridges [5–10]. Xie et al. [11] investigated the high-temperature resistance of carbonise concrete and proposed a constitutive equation for predicting the compressive properties of concrete during high-temperature exposure. The air-void system of concrete determines how well it performs under freezing and thawing situations. Furthermore, in terms of longevity and the mechanical/ physical characteristics of concrete buildings, it is essential to determine the distribution of air holes and pore volume [12].

The interquartile range between a point in concrete mixture and the nearest void's edge is determined by spacing factor, *L*. It is the essential defining characteristic required for safeguarding concrete against thawing and freezing activities. Furthermore, air pore concentration, size, and distribution are important for longevity and concrete buildings' physical/mechanical characteristics [13]. For appropriate design and evaluation of concrete durability and performance in an open environment, accurate measurements of void characteristics and microscope-based standard are required as per ASTM C-457 [14]. ASTM C-457 [14] and its European counterpart EN 480-11 [15] are the most frequently utilised methods for assessing the air void arrangement in concrete at present.

The use of destructive testing procedures to determine compressive strength reduces the cross-section of structural components due to spalling, lowering load bearing capability. These methods are also time-consuming and costly. Instead, quicker and more cost-effective methods for estimating concrete's compressive strength are required. Non- destructive testing like pin penetration, ultrasonic velocity, and pull-off provide estimated findings on concrete compressive strength using numerical formulae involving a series of experiments conducted in a laboratory setting [16–20].

Image processing is the computer-assisted replication of human vision-based activities. Many techniques, like image generation, image digitalisation, categorisation, image augmentation, classification, recording, and imagining, are included in image processing methods [21]. Several studies have been published in the literature that use image processing techniques to analyse concrete's physical and mechanical characteristics. Jennings et al. [22] employed a range of image processing approaches to determine the type of pore structure in back-scattered electron pictures containing bright sections. Two-point correlation and fracture analysis are two image-processing techniques they utilised for dimensioning. Gaydecki et al. [23] employed a portable scanning device with an inductive sensor to identify steel bars embedded in concrete. With this technique, it is able to generate 16-bit gray-leveled images and it is able to extract numerous characteristics about the steel bars buried in concrete using image processing techniques on these pictures. To investigate the mechanical behaviour of concrete, mortar and high-performance concrete specimens under semi-static stress, Huon et al. employed infrared thermography and digital image correlation [22]. Surface polishing, cutting, surface contrasting, and drying take time in the preparation of samples for testing [24–26]. The incorporation of 2D based image techniques using a linear traverse method may not be as representative as the predicted air-void system, since in this method, measurements are limited to one dimension (1D), while air-voids are actually distributed in a three-dimensional (3D) space in hardened concrete. To overcome the limitations mentioned above and to more effectively investigate target materials, a different non-destructive approach which can describe both 2D and 3D objects is needed. X-ray microcomputed tomography (micro-CT) can be used for further investigation of the pore structure of concrete without damaging the material [27–30].

Microcomputed tomography produces a sequence of cross-sectional pictures of the desired material, from which a 3D image is created by stacking 2D images. The three-dimensional dispersion of concrete substances, such as aggregates and pores, may be characterised and analysed in 3D using the micro-CT image produced. The data acquired can be used to explore more complicated studies, like those involving component size and morphology distributions, qualitatively and quantitatively. Micro-CT has been utilised to examine the pore volume of cement composites because of these benefits [31–34].

Most research has utilised volume-based measurement to investigate pore properties using microcomputed tomography, notably pore volume distribution, where the diameter/radius of pores is estimated using the volume of the particle and the formula for estimating sphere volume [10,35–38]. The pore volume distribution of a focused material has been described using the volume-based method by utilising the maximum ball algorithm. Traditional volume-based measurements, presume that pores are completely spherical, limiting their ability to describe anisotropy or variability in pore properties. As a result, a complementary method for characterising pore structures in 3D is required [39]. Several characterisation approaches have been utilised to measure the porous properties of cement-based materials [40–45]. Chord length dispersion is a way to express the geometric features of composite material that may be used to analyse material pore size distribution. Chords are indeed the distances of line crossings with the interfaces, and chord information may be used to calculate the diameter of a pore in a particle. This method allows for a more precise description of particle size properties and pore since it is based on the measured length. Despite its advantages for characterising material properties, chord length distribution has seldom been used to examine the pore architectures of concrete due to its computational difficulty when compared to traditional approaches [46–48].

The pore volume dispersion of concrete specimens of varied air-entraining doses was investigated in this work by utilising varying water/cement ratios. Concrete compressive strength values rise in tandem with the amount of cement in the mix, as is well known. The 2D pore volume dispersion was calculated according to EN 480-11 [49]. The specimens were imaged using micro-CT to produce a series of cross-sectional pictures without causing damage [50]. The specimens' pore volume dispersion was calculated by volume-based technique and the chord-length distribution in 3D using microcomputed tomography images. As a result, grey colour values in concrete pictures are projected to rise. However, this research aims to better understand pore size distribution in cement-based materials. The acquired samples were subjected to mechanical, and durability tests and image processing techniques were employed on samples with identical mixes. Doing so attempted to discover if image analysis may be utilised as an auxiliary approach to disruptive and non-disruptive procedures, as well as the connections between image analysis findings and concrete mechanical strength values. The porosity in concrete samples is the one of the important factor influencing concrete strength character, however pores with diameters smaller than 10 mm has modest effect on the ultimate strength [10]. Due to the specific surface area, there is no discernible influence on strength. The distribution of air-voids in concrete specimens predicted using 3D image technique has excellent precision. Thus, by utilizing the technique of image processing the pore structure of concrete can be investigated without damage to the specimen.

Furthermore, we attempted to determine the cement matrix and ratio of aggregate. The results of the micro-CT scan were compared to the outcomes of the experiment. The efficacy of the investigations employed in this study was proven by demonstrating a link between the pore features acquired and the mechanical strength of the samples. The research findings of Arularasi et al. [51] show that paste and mortar rheological behaviour is identical in the presence of a mineral combination of fly-ash and GGBS

Both cement–fly ash and ternary combinations have relatively better shear and impact resistance as compared to OPC fly-ash based composites [51–57]. Siva et al. [50] conducted experiments to overcome the limitations mentioned above and to more effectively investigate target materials a different non-destructive approach which can describe both 2D and 3D objects is needed. X-ray microcomputed tomography (micro-CT) can be used for further investigation of the pore structure of concrete without damaging the material [24–27]. The work of Jarosław Michałek et al. focuses on methods for evaluating the internal structure of spun concrete that can be used in practise to ensure that the spinning parameters chosen are correct. Following that, imaging techniques and appropriate image processing were used to assess the spatial distribution of pores, aggregate, and cement matrix based on early results reported in [58,59]. Images were used to examine the microstructure of concrete

and forecast its interior properties. For the cost-effective rehabilitation of ageing and disintegrating concrete structures, new approaches for precise and timely condition evaluation, performance prediction, and maintenance management are continually being developed. To this purpose, imaging techniques are becoming more popular due to their high potential for providing accurate information on a structure's viability. To obtain concrete imagery, non-destructive testing techniques such as optical images, which present surface image data, infrared thermography and acoustics, which are used for subsurface conditions, and ground penetrating radar, which is used to obtain below-surface information of a structure, are used. This study provides a technical overview of imaging principles and potential methodologies for the automated identification, measurement, and characterization of pores in concrete.

2. Materials and Methods

2.1. Materials Preparation of Test

This study employed aggregate and sand ingredients to make the concrete sample. The aggregates came in two kinds (sandstone and limestone) and were in their original, undisturbed state. Table 1 shows the chemical properties of the cement used in concrete. According to ACI 2111-91 [60], the volumetric technique developed and produced concrete mixes in the laboratory. Tables 1–5 shows the properties of cement, fly-ash and aggregates obtained from Astra Chemicals.

Table 1. Properties of cement.

Material	Physical Properties	Test Result
Ordinary portland cement 53 Grade	Consistency (%)	26
	Initial Setting Time (min)	179
	Final Setting Time (min)	289
	Fineness dry sieving (%)	5.1
	Compressive Strength N/mm^2	18.2 MPa (3 days) 37.5 MPa (7 days) 56.8 MPa (28 days)

Table 2. Properties of coarse aggregate.

Material	Physical Properties	Test Result
Coarse Aggregate	Specific Gravity	2.80
	Soundness	2.58
	Moisture Content	0.11
	Water Absorption (%)	0.56
	Bulk Density Loose (kg/m^3)	1506
	Bulk Density Rodded (kg/m^3)	1750

Table 3. Properties of crushed stone aggregate.

Material	Physical Properties	Test Result
Crushed Stone Aggregate (FA)	Specific Gravity	2.72
	Bulking (%)	9.55
	Moisture Content	0.31
	Water Absorption (%)	2.07
	Bulk Density (kg/m^3)	1668
	Silt Content	1.34
	Soundness	1.13

Table 4. Properties of fly-ash.

Material	Physical Properties	Test Result IS 3812:2017
Fly-ash	Normal Consistency, (%)	30.5%
	Initial Consistency Setting Time, (min)	193
	Final Setting Time, (min)	429
	Strength Index with Cement	54.2
	Dry Density (g/cc)	1.4
	Plasticity	Non-Plastic

Table 5. Oxides of cement and fly-ash.

Oxides	Al_2O_3	CaO	SiO_2	Fe_2O_3	K_2O	MgO	SO_3	Cl	TiO_2
Cement %	3.2	71.1	15.8	5.4	0.8	0.7	2.15	0.25	0.6
Fly-ash %	28.9	1.8	57.4	5.8	2.1	0.6	0.9	0.27	2.21

The coarse aggregate size chosen was 20 mm. The fine aggregate particle size distribution is shown in Figure 1. The mix FA5C95 denotes 5% of fly-ash and 95% of cement. The M20 concrete mix was manufactured according to IS10262:2009, with a mix design ratio of 1:1.5:2.9 and a w/c ratio of 0.47. The flow table test was used to measure the consistency of fresh concrete, and the findings showed that it was within the specified range of 390–440 mm. Density of concrete increases as fly-ash content increased. The fresh density of the reference mix (without fly-ash) was 2083.4 kg/m^3, which steadily increased to 2325 kg/m^3 as the amount of fly-ash in the mixture was increased. The moulds were placed on a vibrating table, the produced new concrete was poured in two layers of 50 mm thick in cubic moulds of $100 \times 100 \times 100$ mm^3 in accordance with ACI 2111-91 [60] and in cylindrical moulds of 100×200 mm^2 in consonance with ASTM C-192 [61]. After 24 h, the samples were demolded and kept underwater for curing at a constant temperature (20 °C) until the testing day. Hardened concrete parameters, such as dry state density, compressive strength, water porosity, and water permeability (EN 12390-8), were determined after 28 days the results are shown in Table 6. Four cubic concrete specimens were prepared for 28-day mechanical strength testing, and one specimen was utilized to create computed tomography pictures. The fine and coarse aggregates were first placed into the mixer, followed by the water and cement, and then combined for five minutes. The cubic specimens were subjected to uniaxial compressive strength testing in compliance with the British standard.
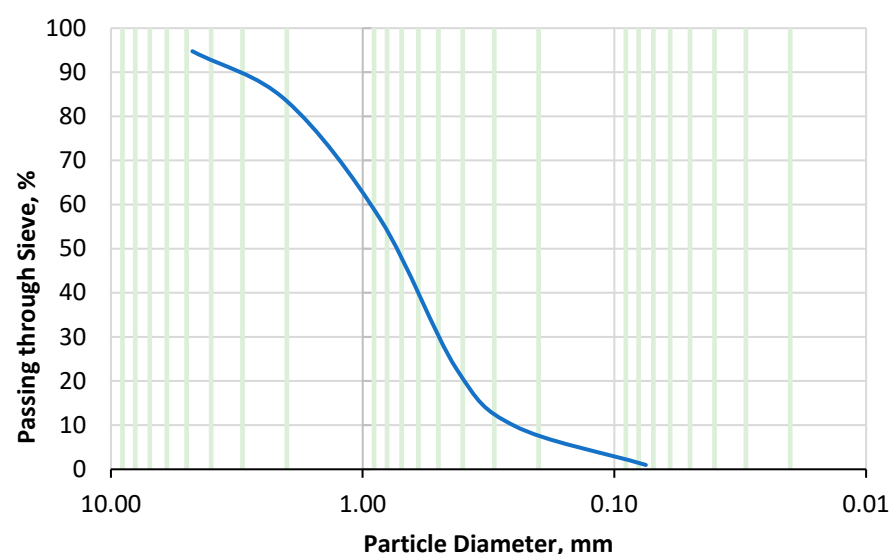

Figure 1. Particle size distribution gradation curve.

Table 6. Properties and compressive strength of test specimens.

Mixes	Dry Density	Water Porosity	Water Penetration	Compressive Strength (MPa)		
	Kg/m^3	Vol.%	mm	7 days	14 days	28 days
Control Sample	2083.4	9.9 $\pm$ 0.3	52	12.99	19.17	20.14
FA5C95	2137	9.8 $\pm$ 0.3	39	12.51	19.31	20.3
FA10C90	2197.9	9.7 $\pm$ 0.3	31	12.19	20.03	20.98
FA15C85	2269	9.7 $\pm$ 0.3	25	11.71	20.03	20.78
FA20C80	2325	9.6 $\pm$ 0.3	16	11.63	19.46	20.17

To assess the pore size distribution and pore properties of materials [33,62] a standardised 2D SEM imaging approach was used. Two-dimensional projections were used to determine the 2D morphological properties of concrete. Reconstructed multiphysics models were used to obtain 3D morphological properties. A JOEL scanning electron microscope was used to take the SEM images (JSM-IT800). The image processing method was modified to examine the percentages of air gaps, cement matrix, and aggregate dispersion in concrete. To construct 2D and 3D multiphysics model images, a succession of 2D X-ray photographs was used. The inner structure of a specimen can be studied using 2D and 3D images [5]. The Weibull [63,64] and lognormal [26] fits were used to describe the pore size distribution. The test sample images are shown in Figure 2, and a high-definition camera with a range of 12.2 pixels was used to image cut concrete surfaces. After taking the specimens from the water, the surfaces were dried and shot in RGB colour mode with a 4272 $\times$ 2848-pixel resolution. All photographs of concrete samples were taken at the same distance from the sample surface and with the same light intensity.

(a) (b)
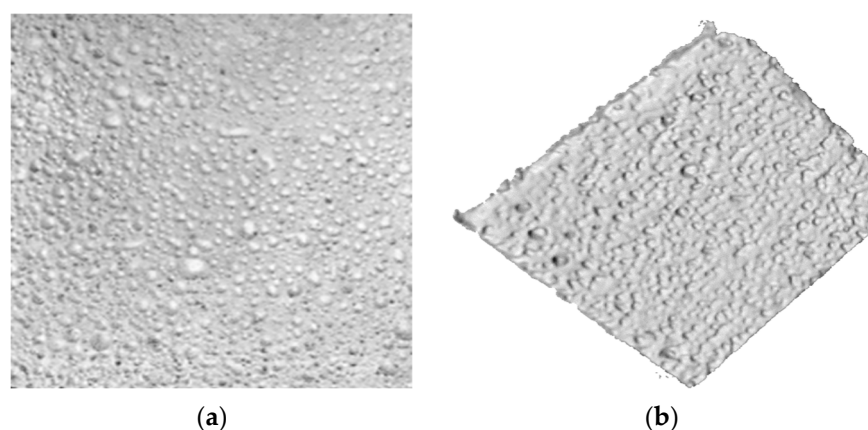
Figure 2. Two-dimensional (2D) image of concrete specimens. (**a**) Concrete surface original image, (**b**) sample surface 3D structure.

2.2. Measurement Tools

The image data were processed using MATLAB, (MathWorks, Natick, MA, USA). First, the 16-bit images are transformed to an 8-bit TIFF format to minimize computational complexity, because the square matrix provides the foundation for image creation.

2.3. Porosity Measurement by Image Processing Technique

The surface of the material was analysed and characterised using a standardized 2D SEM image-based method. The scanning electron microscope (SEM) is a non-destructive microscopy solution technique that creates images by interacting with atoms on the sample's surface and a beam of electrons [65]. This aids in the provision of information on the sample's surface properties and composition. It also aids in the reconstruction of the surface morphology of a sample [65]. The scanning electron microscope (SEM) is the only

direct observational approach that gives high-resolution pictures that may be used to analyse the differences between pore space features and mineral matrix details [66]. Despite the fact that there are three types of signal available, secondary electrons, backscattered electrons and X-rays, the backscattered electron detector is chosen in this investigation since it eliminates any errors in porosity estimation [67]. To prevent the sample from charging during analysis, the surface of the rock sample was coated with gold [68]. With a 5.00 kV accelerating voltage, SEM imaging was performed. X-rays were used in a radiographic imaging approach to study the material's interior structure; X-rays were used in a radiographic imaging approach. A pixel in a 2D SEM picture is made up of 8- to 16-bit grayscale digital image, which creates deep map-based image and binary segmented image. For a clear description of single pore colour, a modified deep mapping technique was applied, which yielded a value multiplied by 100%. These computations were carried without taking into consideration the areas that were exposed in the segmented pictures, as shown in Figure 3.
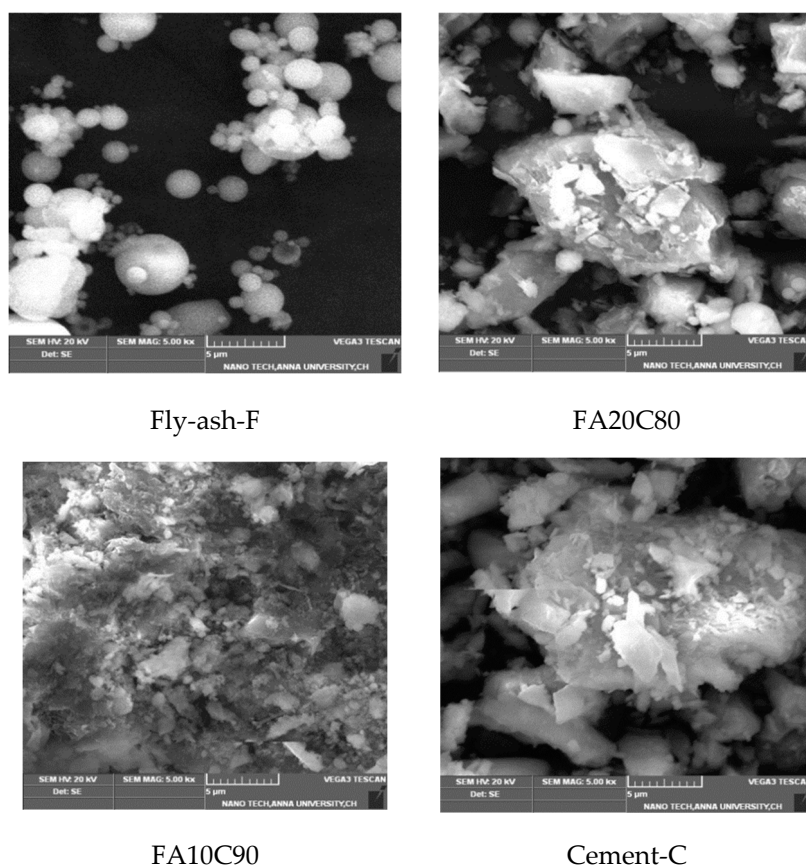

Fly-ash-F

FA20C80

FA10C90

Cement-C

Figure 3. Micro-CT (computed tomography) image.

Because the SEM images were grayscale, the pore regions were revealed by the black spots of the binary segmentation picture, and a frequency plot of pore volume distribution was created. The pore volume distribution of the specimen was investigated using a 2D SEM image technique, with the pore size distribution being quantified by volume-based methods integrated into the picture. The MATLAB imaging toolbox was used to do all of the picture processing.

Figure 4 shows the binary image of sample images with only two possible intensity values are known as binary images. In terms of numbers, black is usually 0 and white is usually 1 or 255. Binary pictures are particularly valuable in the field of image processing because they make it simple to distinguish an air pores from the materials surrounding. The segmentation method allows each pixel to be labelled as "background" or "object", with

black and white colours assigned to each. The chord length function may be used to describe the properties of random heterogeneous materials in 2D in general. However, merely using 2D pictures to describe a target material's general properties has limits, especially for samples with specialized components like anisotropic pores. As a result, 3D pictures are required for a more detailed and precise characterization of a target material. In this work, 3D micro-CT images using SKYSCAN 2214 were used to evaluate the pore volume dispersion of air-entrained concrete specimens by both volume-based approach and chord length distribution. The three-dimensional pore volume dispersion was then compared.
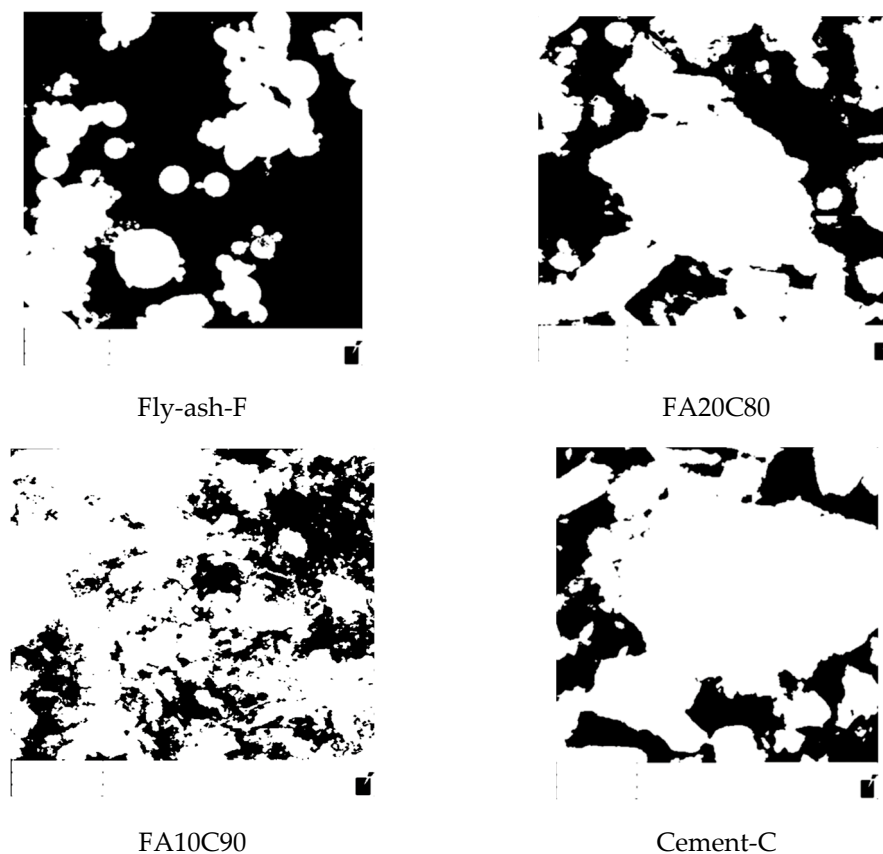

Fly-ash-F

FA20C80

FA10C90

Cement-C

Figure 4. Binarised image.

3. Results and Discussion

3.1. Compressive Strength

Table 5 and Figure 4 illustrate the influence of fly-ash on concrete's mechanical properties after 7, 14, and 28 days. At later ages, the usage of fly-ash for cement as a binder produces higher mechanical strength values than the control specimen. The compressive strengths of specimens containing fly-ash were compared to the control Specimen in Table 3. Figure 5 shows that after seven days of curing, the compressive strengths of the concrete specimen containing fly-ash were lesser than those of the control specimen. FA5C95 seemed to have the maximum mechanical strength after 7 days of curing, whereas FA20C80 had the lowest. The quantity of fly-ash added to the mix increased, but the compressive strength drops, this the trend pattern continues linearly till 7 days.
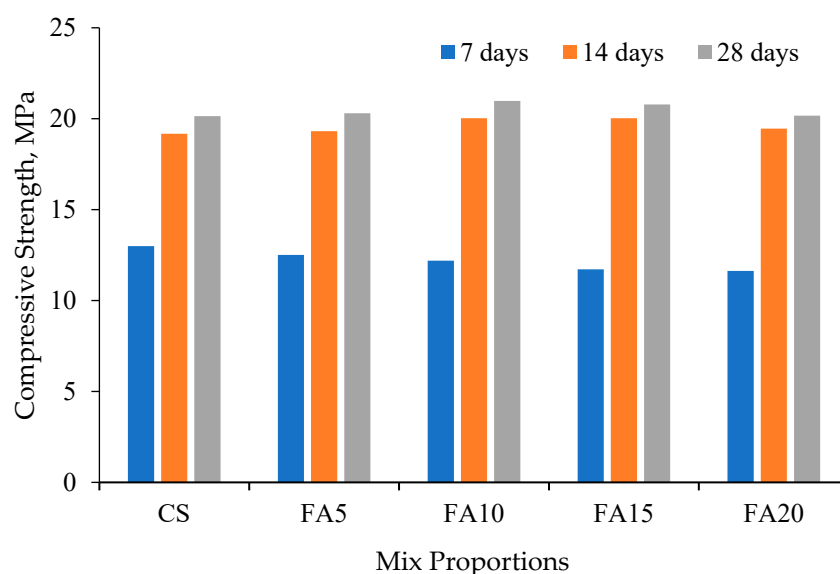
Figure 5. Comparison of specimen compressive strength.

The compressive strengths of concrete mixes containing various percentages of fly-ash were typically greater than those of the control specimen after the curing of 28 days. FA10C90 had the highest compressive strength in this group, whereas Control specimen had the lowest compressive strength. The compressive strength of FA20C80 was similar to control specimen when the fly-ash ratio was greater than 10% by weight of cement. Fly ash-containing concrete mixes had higher compressive strengths than the control sample.

After 28 days of curing, the FA10C90 specimens had a high mechanical strength than the other specimens, whereas the control specimens had less mechanical strength. The mechanical strength of the FA20C80 specimens decreased after 28 days at the fly-ash ratio was more than 10%. When the observations were investigated, it was revealed that the compressive strengths at 7, 14, 28 days of age were decreasing at all ratios. The quantity of fly-ash in concrete enhanced the mechanical strength of all mix combinations. Since the size of the particles of fly-ash is relatively small than that of cement, it fills the void at the aggregate–cement interface. In contrast, the hydrates of oxides in fly-ash accelerate the pozzolanic reaction [69–71].

3.2. Material Properties

Concrete mixes are produced and evaluated in this research to investigate the microstructure and porosity of concrete using various assessment methods. The fresh concrete properties were determined from consistency, fresh density, and air content. The properties of hardened concrete, including dry density, open porosity (water porosity), water penetration depth, and 28-day compressive strength, were determined from experimental results. The findings of water porosity and permeability show that a high air content in concrete has a detrimental influence on its transport characteristics. Differences between optimal moisture content samples and oven-dried samples were utilised to calculate water porosity. Because the air bubbles injected had the properties of closed pores, which did not actually assist in the capillary transmission of liquid water under normal conditions, there were no significant variations between specimens in terms of water porosity. Compressive strength tests were conducted to assess the impact of rising air concentration on the mechanical characteristics of concrete. The data show that when the air content increased, strength decreased substantially. Compressive strength was shown to be reduced when the fly-ash ratios were increased in our study. This is because surface morphology, comprising porosity and pore size distribution, can substantially impact mechanical properties.

Two-dimensional and three-dimensional methods were used to analyse the specimens' pore size distributions. The chord-length-based and volume-based techniques integrating

micro chromatography images were used to measure the pore volume dispersion in 3D. Chord length distribution [72] is a method for characterising the morphological information of material properties that can be used to analyse the pore size distribution of materials. Chords are the distances between line intersections with the interface [48], and chord information can be used to calculate the radius of a target pore. Most investigations employing micro-CT to investigate pore features, notably pore size distribution, have used volume-based measurement, in which the radius (or diameter) of pores is estimated from the particle volume and the sphere volume formula [35]. The pore size distribution of a target material has been described using volume-based techniques such as the Weibull and lognormal maximum ball algorithm [39]. Figure 6 shows the 3D pictures of the pore structures for each specimen. The grey coloured particles in this picture indicate the pores within the samples, and the pore structure analysis was undertaken using this data. From the porosity values of the specimens in Table 7, it can be deduced that the porosity, average pore radius, and fracture surface of the sample are comparable, as validated by image processing. The pore volume dispersion of the specimens are compared, with pore volume dispersion produced using various methods superimposed. Because the equipment meets the applicable requirements, the data were used as a reference. The pore size distributions of the specimens are shown in Figure 7, with the pore size distributions obtained overlaid. The frequency of pore size in the specimens is shown on the y-axis. The regions of the graphs tended to grow as the air content of the specimen increased. The pore volume dispersion in Figures 6 and 8 demonstrate that the main patterns in all surface measurements instances were comparable. The areas of the graphs tended to rise with an increase in the air gap content of the specimen for all measurement techniques. When compared to the micro-CT method, the size dispersion of tiny holes revealed a similar pattern in all cases. The dual-modal distributions were not clearly seen in the volumetric measurement. Because all holes are assumed to be spheres in volume-based measurements, heterogeneous or anisotropic pores might look smaller than they are in some directions; the micro-CT revealed a similar pattern, suggesting it could contribute to a greater understanding of material properties.

The applicability of estimating concrete pore dispersion using microstructure images analysis was investigated in this study. The compressive strength of concrete structures is substantially determined by the thickness of the interfacial transition zone, as well as the presence of micro-cracks and pores. This indicates that the microstructure pictures of concrete and compressive strength are interrelated. As a result, by evaluating images of the concrete microstructure, this study sought to determine pore volume of concrete. The validity of the air-void parameters obtained from micro CT imaging is assessed in this section. Air content and spacing variables are inversely proportional to one another [73]. Despite the fact that the relationship is not highly connected, it can be used to validate the values of the parameters acquired in this study. The link between air content and spacing parameters derived from this study was superimposed on data from the literature [73–75] and the results demonstrate high quantitative agreement with previously reported data. By reconstructing sliced images and determining the pore spacing factor in 3D space, as described by Powers [76], the characterization of 3D air-void configuration may be done. The equations proposed in ASTM C457 were created using the stereology principle, which seeks to estimate 3D properties based on a 2D inspection when 3D information is unavailable. The pore spacing factor was described as half the distance between two diagonally adjacent voids in an assembly, assuming all voids are mono-sized spheres evenly scattered across the volume [76]. Due to the fact that this distance cannot be determined using traditional optical methods, the stereology-based linear-traverse approach or modified count methods have been commonly utilised to estimate the spacing factor. Unlike optical technologies, however, micro CT allows for the identification of air gaps and the calculation of the pores in 3D space.
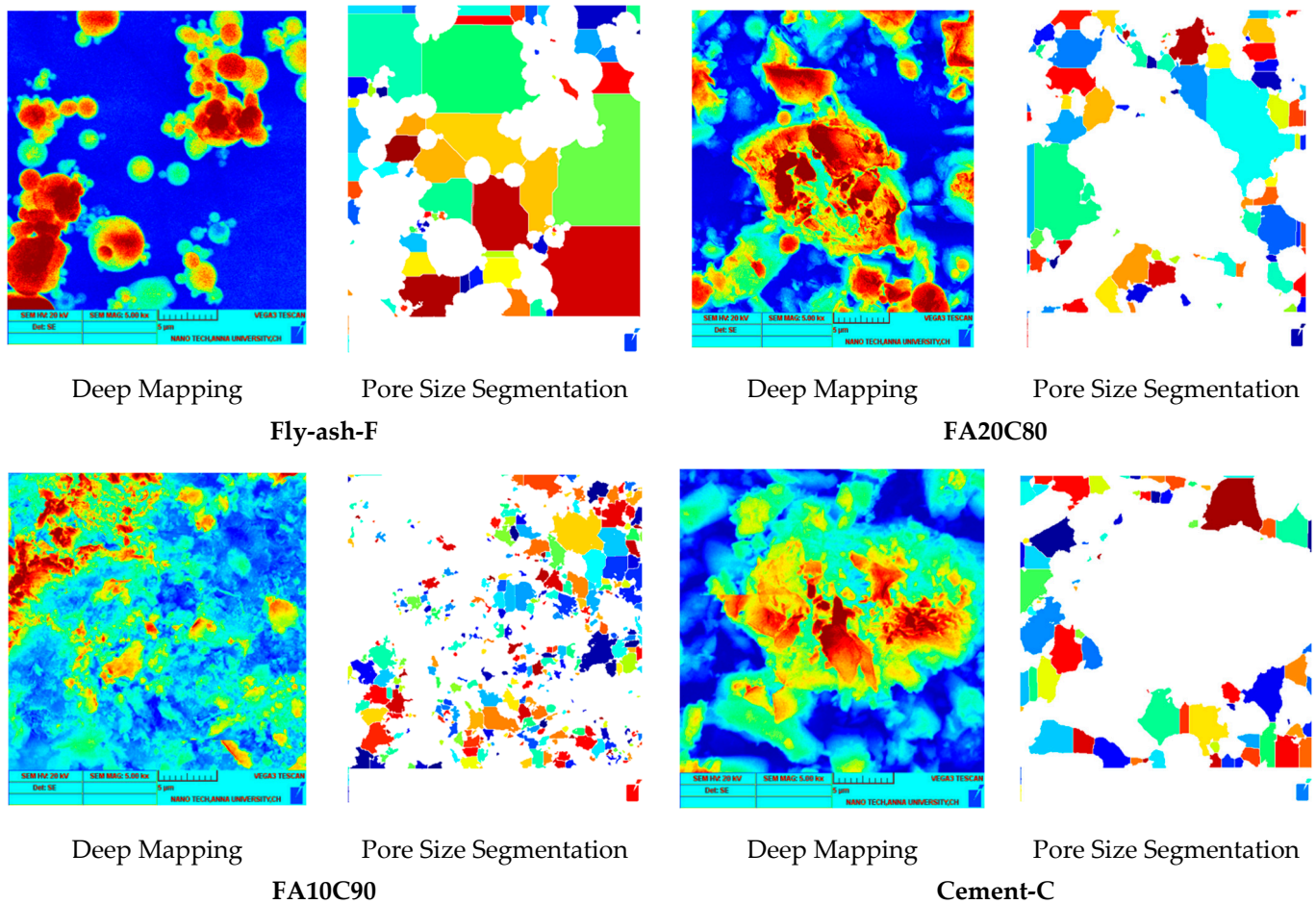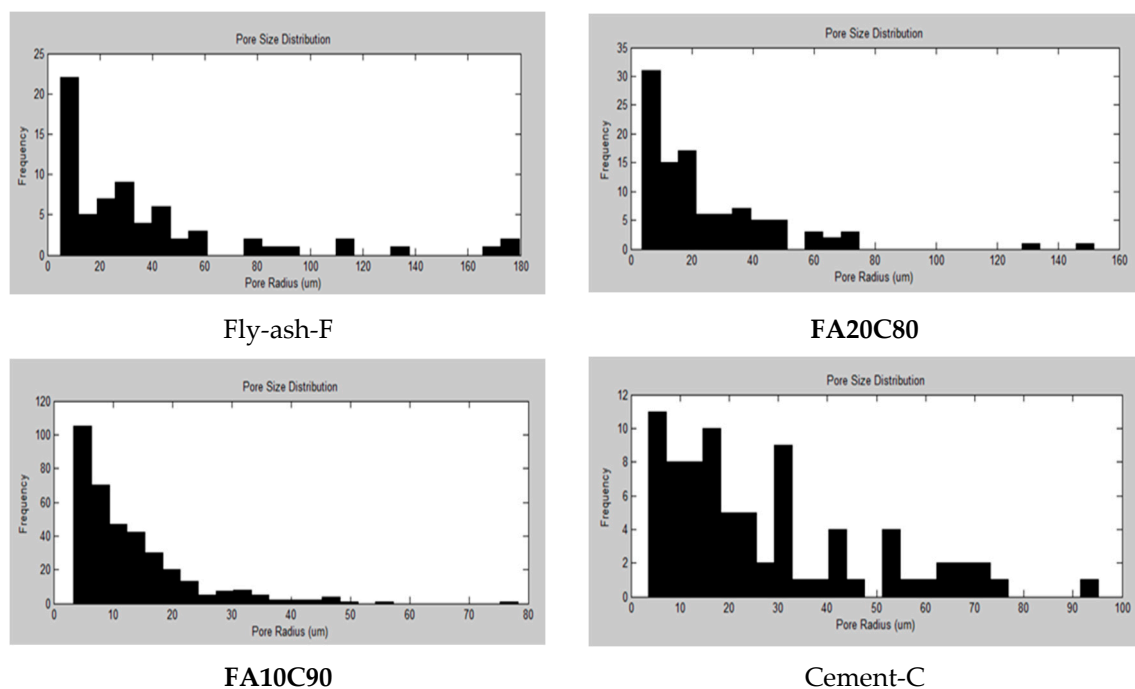
Figure 6. Micro-structural image processing.

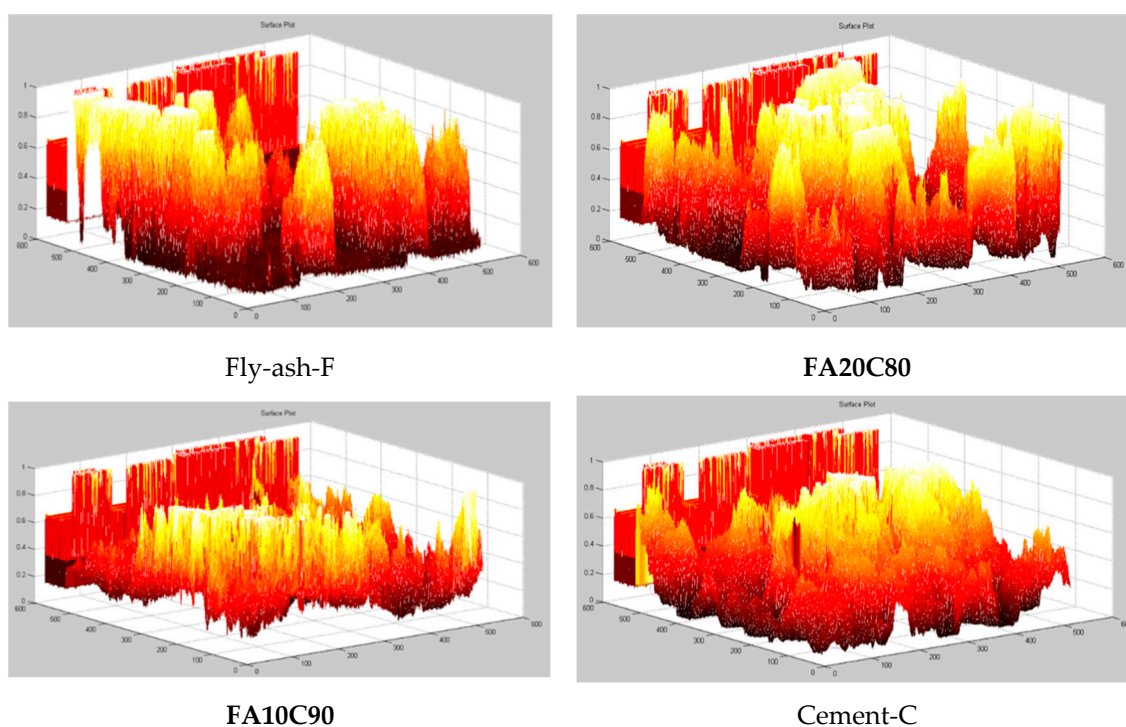Figure 7. Pore size distribution for different samples.

Fly-ash-F

FA20C80

FA10C90

Cement-C

Figure 8. Comparison of surface measurements for different samples.

Table 7. Confirmation of concrete crack by porosity measurements.

Parameters	Fly-Ash	FA20C80	FA5C95	Cement
Porosity (%)	0.5602	0.3384	0.2699	0.2528
Average pore radius (μm)	37.7422	24.9382	12.8812	27.1833
Standard deviation of pore radius	40.4022	24.4782	9.9723	20.9451

4. Conclusions

Micro-CT is a reliable method for determining the microstructural configuration of materials in a non-destructive, high-resolution way. The use of X-ray CT imaging to determine the air-void characteristics of cement-based materials has been discussed in this work. The following are some of the benefits of micro-CT imaging. This approach does not necessitate any physical preparation of the specimens, such as cutting and polishing. Second, by limiting sampling effects, the approach can improve the representativeness of the parameters, allowing for quantification of air-void distribution heterogeneity. Image processing techniques were utilised to describe the pore volume dispersion of the sample, revealing that range of pores in concrete specimens. The experiment's efficiency was demonstrated by the relation between the pore characteristics determined and the compressive strength of the specimens.

Chord-length-based pore size characteristics are nearly equivalent to those determined using the traditional 2D technique. The incorporation of 3D microstructure chromatography in this study helps to describe the pore size distribution more effectively.

- Although the Weibull and lognormal distributions have been used to characterise pore size distributions, both techniques are limited when a material possesses a substantial percentage of larger pores.
- Pore volume dispersion has been described using the Weibull and lognormal distributions, but both approaches are restricted when a material has a high proportion of relatively large pores. A bimodal (or multimodal) normal distribution can be used to characterise the pore size distribution of a material with peak intensity produced by big pores.

– When compared to the standardised method, the systematic evaluation method developed and verified in this research revealed good accuracy and correlation, and this methodology can be used to manufacture advanced construction materials with specific pore parameters.

– It is also found that the compressive strength of FA20C80 was similar to control specimen when the fly-ash ratio was greater than 10% by weight of cement. Fly ash-containing concrete mixes had higher compressive strengths than the control sample.

– The investigation's accuracy was observed by the relationship between the pore characteristics discovered and the compressive strength of the specimens.

– In addition to the study's concluding observations, more parametric studies with various fly-ash dosages and formulations need to be conducted to gain a better knowledge of pore size distribution and its relationship to material factors.

Furthermore, it can be clarified that the next phase of this research is to use waste materials/filler, to predict the pore volume dispersion and microstructural characteristics of concrete using an image processing technique.

Author Contributions: Conceptualization, D.K.; Data curation, M.J., S.A., M.A., R.A., R.F. and N.V.; Formal analysis, D.K., M.J., S.A., M.A., R.A., R.F. and N.V.; Funding acquisition, M.A. and R.F.; Investigation, D.K. and M.J.; Methodology, D.K. and M.J.; Project administration, M.A. and N.V.; Resources, S.A., M.A., R.F. and N.V.; Software, R.A., R.F. and N.V.; Supervision, S.A.; Validation, M.A., R.A., R.F. and N.V.; Visualization, S.A., M.A., R.A. and N.V.; Writing—original draft, D.K. and M.J.; Writing—review and editing, S.A., M.A., R.A., R.F. and N.V. All authors have read and agreed to the published version of the manuscript.

Institutional Review Board Statement: Not applicable.

Informed Consent Statement: Not applicable.

Data Availability Statement: Data sharing not applicable.

Conflicts of Interest: The authors declare no conflict of interest.

References

1. Odler, I.; Rößler, M. Investigations on the relationship between porosity, structure and strength of hydrated Portland cement pastes. II. Effect of pore structure and of degree of hydration. *Cem. Concr. Res.* **1985**, *15*, 401–410. [CrossRef]

2. Kumar, R.; Bhattacharjee, B. Porosity, pore size distribution and in situ strength of concrete. *Cem. Concr. Res.* **2003**, *33*, 155–164. [CrossRef]

3. Diamond, S. A critical comparison of mercury porosimetry and capillary condensation pore size distributions of portland cement pastes. *Cem. Concr. Res.* **1971**, *1*, 531–545. [CrossRef]

4. Xie, Q.; Yang, L.; Hu, F.; Hao, W.; Yin, S.; Zhang, L. Degradation Behavior of Concrete after Freeze-Thaw Cycles and Then Exposure to High Temperatures. *Adv. Mater. Sci. Eng.* **2019**, *2019*, 9378935. [CrossRef]

5. Chung, S.-Y.; Sikora, P.; Rucinska, T.; Stephan, D.; Abd Elrahman, M. Comparison of the pore size distributions of concretes with different air-entraining admixture dosages using 2D and 3D imaging approaches. *Mater. Charact.* **2020**, *162*, 110182. [CrossRef]

6. Sidney Mindess, J.; Francis Young, D.D. *Concrete*, 2nd ed.; Pearson Education Inc.: Upper Saddle River, NJ, USA, 2003; Volume 1, pp. 1–476.

7. Maia, L.; Figueiras, J. Early-age creep deformation of a high strength self-compacting concrete. *Constr. Build. Mater.* **2012**, *34*, 602–610. [CrossRef]

8. Chopra, P.; Sharma, R.K.; Kumar, M. Prediction of Compressive Strength of Concrete Using Artificial Neural Network and Genetic Programming. *Adv. Mater. Sci. Eng.* **2016**, *2016*, 7648467. [CrossRef]

9. Chahal, N.; Siddique, R.; Rajor, A. Influence of bacteria on the compressive strength, water absorption and rapid chloride permeability of fly ash concrete. *Constr. Build. Mater.* **2012**, *28*, 351–356. [CrossRef]

10. Amran, M.; Fediuk, R.; Murali, G.; Vatin, N.; Al-Fakih, A. Sound-Absorbing Acoustic Concretes: A Review. *Sustainability* **2021**, *13*, 10712. [CrossRef]

11. Xie, Q.; Zhang, L.; Yin, S.; Zhang, B.; Wu, Y. Effects of High Temperatures on the Physical and Mechanical Properties of Carbonated Ordinary Concrete. *Adv. Mater. Sci. Eng.* **2019**, *2019*, 5753232. [CrossRef]

12. Moravcová, B.; Põssl, P.; Misák, P.; Blažek, M. Possibilities of determining the air-pore content in cement composites using computed tomography and other methods. *Mater. Tehnol.* **2016**, *50*, 491–498. [CrossRef]

13. Mehta, P.K. *Concrete: Structure, Properties and Materials*, 3rd ed.; McGraw-Hill: New York, NY, USA, 2006; ISBN 9789896540821.

14. Wolter, S.; Uhre, F.A.H.; Hasholt, M.T.; Dahl, V.A.; Anton, F. Air void analysis of hardened concrete by means of photogrammetry. *Constr. Build. Mater.* **2019**, *226*, 953–964. [CrossRef]

15. *BS EN 480-5:2005 Admixtures for Concrete, Mortar and Grout—Test Methods Part 5: Determination of Capillary Absorption*; British Standards Institution: London, UK, 2005; Volume 3, pp. 3–36.

16. Hassan, A.M.T.; Jones, S.W. Non-destructive testing of ultra high performance fibre reinforced concrete (UHPFRC): A feasibility study for using ultrasonic and resonant frequency testing techniques. *Constr. Build. Mater.* **2012**, *35*, 361–367. [CrossRef]

17. Topçu, İ.B.; Sarıdemir, M. Prediction of compressive strength of concrete containing fly ash using artificial neural networks and fuzzy logic. *Comput. Mater. Sci.* **2008**, *41*, 305–311. [CrossRef]

18. Demirboğa, R.; Türkmen, I.; Karakoç, M.B. Relationship between ultrasonic velocity and compressive strength for high-volume mineral-admixtured concrete. *Cem. Concr. Res.* **2004**, *34*, 2329–2336. [CrossRef]

19. Taketo Uomoto—Non-Destructive Testing in Civil Engineering 2000-Elsevier Science (2000).pdf. Available online: http://reeceregoloben.s3.amazonaws.com/32/non-destructive-testing-in-civil-engineering-2000-uomoto-t-dbid-2bqq0.pdf (accessed on 20 November 2021).

20. Akkoyun, O. An evaluation of image processing methods applied to marble quality classification. In Proceedings of the 2010 2nd International Conference on Computer Technology and Development, Cairo, Egypt, 2–4 November 2010; pp. 158–162.

21. Başyiğit, C.; Çomak, B.; Kılınçarslan, Ş.; Serkan Üncü, İ. Assessment of concrete compressive strength by image processing technique. *Constr. Build. Mater.* **2012**, *37*, 526–532. [CrossRef]

22. Lange, D.A.; Jennings, H.M.; Shah, S.P. Image analysis techniques for characterization of pore structure of cement-based materials. *Cem. Concr. Res.* **1994**, *24*, 841–853. [CrossRef]

23. Gaydecki, P.; Silva, I.; Fernandes, B.T.; Yu, Z.Z. A portable inductive scanning system for imaging steel-reinforcing bars embedded within concrete. *Sens. Actuators A Phys.* **2000**, *84*, 25–32. [CrossRef]

24. Huon, V.; Cousin, B.; Wattrisse, B.; Maisonneuve, O. Investigating the thermo-mechanical behaviour of cementitious materials using image processing techniques. *Cem. Concr. Res.* **2009**, *39*, 529–536. [CrossRef]

25. Trubić, A.H.; Mikulić, D.; Uzelac, S. Concrete resistance to freezing and thawing effects. *Teh. Vjesn.* **2009**, *16*, 63–74.

26. Kim, K.Y.; Yun, T.S.; Choo, J.; Kang, D.H.; Shin, H.S. Determination of air-void parameters of hardened cement-based materials using X-ray computed tomography. *Constr. Build. Mater.* **2012**, *37*, 93–101. [CrossRef]

27. Chotard, T.J.; Boncoeur-Martel, M.P.; Smith, A.; Dupuy, J.P.; Gault, C. Application of X-ray computed tomography to characterise the early hydration of calcium aluminate cement. *Cem. Concr. Compos.* **2003**, *25*, 145–152. [CrossRef]

28. Patterson, B.M.; Escobedo-Diaz, J.P.; Dennis-Koller, D.; Cerreta, E. Dimensional Quantification of Embedded Voids or Objects in Three Dimensions Using X-Ray Tomography. *Microsc. Microanal.* **2012**, *18*, 390–398. [CrossRef] [PubMed]

29. Chung, S.-Y.; Han, T.-S. Correlation between low-order probability distribution functions and percolation of porous concrete. *Mag. Concr. Res.* **2013**, *65*, 448–460. [CrossRef]

30. Natesaiyer, K.; Chan, C.; Sinha-Ray, S.; Song, D.; Lin, C.L.; Miller, J.D.; Garboczi, E.J.; Forster, A.M. X-ray CT imaging and finite element computations of the elastic properties of a rigid organic foam compared to experimental measurements: Insights into foam variability. *J. Mater. Sci.* **2015**, *50*, 4012–4024. [CrossRef]

31. Su, Y.-M.; Hossiney, N.; Tia, M. The analysis of air voids in concrete specimen using X-ray computed tomography. In Proceedings of the Nondestructive Characterization for Composite Materials, Aerospace Engineering, Civil Infrastructure, and Homeland Security 2013, San Diego, CA, USA, 16 April 2013; Volume 8694, p. 86940S. [CrossRef]

32. Chung, S.-Y.; Elrahman, M.A.; Stephan, D.; Kamm, P.H. Investigation of characteristics and responses of insulating cement paste specimens with Aer solids using X-ray micro-computed tomography. *Constr. Build. Mater.* **2016**, *118*, 204–215. [CrossRef]

33. Bossa, N.; Chaurand, P.; Vicente, J.; Borschneck, D.; Levard, C.; Aguerre-Chariol, O.; Rose, J. Micro- and nano-X-ray computed-tomography: A step forward in the characterization of the pore network of a leached cement paste. *Cem. Concr. Res.* **2015**, *67*, 138–147. [CrossRef]

34. da Silva, Í.B. X-ray Computed Microtomography technique applied for cementitious materials: A review. *Micron* **2018**, *107*, 1–8. [CrossRef]

35. Yun, T.S.; Kim, K.Y.; Choo, J.; Kang, D.H. Quantifying the distribution of paste-void spacing of hardened cement paste using X-ray computed tomography. *Mater. Charact.* **2012**, *73*, 137–143. [CrossRef]

36. Yuan, J.; Wu, Y.; Zhang, J. Characterization of air voids and frost resistance of concrete based on industrial computerized tomographical technology. *Constr. Build. Mater.* **2018**, *168*, 975–983. [CrossRef]

37. Lu, H.; Peterson, K.; Chernoloz, O. Measurement of entrained air-void parameters in Portland cement concrete using micro X-ray computed tomography. *Int. J. Pavement Eng.* **2018**, *19*, 109–121. [CrossRef]

38. Chung, S.Y.; Elrahman, M.A.; Sikora, P.; Rucinska, T.; Horszczaruk, E.; Stephan, D. Evaluation of the effects of crushed and expanded waste glass aggregates on the material properties of lightweight concrete using image-based approaches. *Materials* **2017**, *10*, 1354. [CrossRef] [PubMed]

39. Dong, H.; Blunt, M.J. Pore-network extraction from micro-computerized-tomography images. *Phys. Rev. E* **2009**, *80*, 36307. [CrossRef] [PubMed]

40. Fedyuk, R.S.; Baranov, A.; Mugahed Amran, Y.H. Effect of porous structure on sound absorption of cellular concrete. *Constr. Mater. Prod.* **2020**, *3*, 5–18. [CrossRef]

41. Amran, Y.H.M. Influence of structural parameters on the properties of fibred-foamed concrete. *Innov. Infrastruct. Solut.* **2020**, *5*, 1–18. [CrossRef]

42. Lesovik, V.; Voronov, V.; Glagolev, E.; Fediuk, R.; Alaskhanov, A.; Amran, Y.H.M.; Murali, G.; Baranov, A. Improving the behaviors of foam concrete through the use of composite binder. *J. Build. Eng.* **2020**, *31*, 101414. [CrossRef]

43. Amran, M.; Fediuk, R.; Vatin, N.; Lee, Y.H.; Murali, G.; Ozbakkaloglu, T.; Klyuev, S.; Alabduljabber, H. Fibre-reinforced foamed concretes: A review. *Materials* **2020**, *13*, 4323. [CrossRef]

44. Mugahed Amran, Y.H.; Alyousef, R.; Alabduljabbar, H.; Khudhair, M.H.R.; Hejazi, F.; Alaskar, A.; Alrshoudi, F.; Siddika, A. Performance properties of structural fibred-foamed concrete. *Results Eng.* **2020**, *5*, 100092. [CrossRef]

45. Abid, S.R.; Murali, G.; Amran, M.; Vatin, N.; Fediuk, R.; Karelina, M. Evaluation of mode II fracture toughness of hybrid fibrous geopolymer composites. *Materials* **2021**, *14*, 349. [CrossRef]

46. Torquato, S.; Haslach, H.W., Jr. Random Heterogeneous Materials: Microstructure and Macroscopic Properties. *Appl. Mech. Rev.* **2002**, *55*, B62–B63. [CrossRef]

47. du Plessis, A.; Olawuyi, B.J.; Boshoff, W.P.; le Roux, S.G. Simple and fast porosity analysis of concrete using X-ray computed tomography. *Mater. Struct. Constr.* **2016**, *49*, 553–562. [CrossRef]

48. Torquato, S.; Lu, B. Chord-length distribution function for two-phase random media. *Phys. Rev. E Stat. Phys. Plasmas Fluids Relat. Interdiscip. Top.* **1993**, *47*, 2950–2953. [CrossRef]

49. *ASTM C 457/C 457M-12 Standard Test Method for Microscopical Determination of Parameters of the Air-Void System in Hardened Concrete 1*; ASTM International: West Conshehoken, PA, USA, 2013; Volume 5, pp. 1–15. [CrossRef]

50. Avudaiappan, S.; Prakatanoju, S.; Amran, M.; Aepuru, R.; Saavedra Flores, E.I.; Das, R.; Gupta, R.; Fediuk, R.; Vatin, N. Experimental Investigation and Image Processing to Predict the Properties of Concrete with the Addition of Nano Silica and Rice Husk Ash. *Crystals* **2021**, *11*, 1230. [CrossRef]

51. Arularasi, V.; Thamilselvi, P.; Avudaiappan, S.; Flores, E.I.S.; Amran, M.; Fediuk, R.; Vatin, N.; Karelina, M. Rheological behavior and strength characteristics of cement paste and mortar with fly ash and GGBS admixtures. *Sustainability* **2021**, *13*, 9600. [CrossRef]

52. Amran, M.; Debbarma, S.; Ozbakkaloglu, T. Fly ash-based eco-friendly geopolymer concrete: A critical review of the long-term durability properties. *Constr. Build. Mater.* **2021**, *270*, 121857. [CrossRef]

53. Amran, Y.H.M.; Soto, M.G.; Alyousef, R.; El-Zeadani, M.; Alabduljabbar, H.; Aune, V. Performance investigation of high-proportion Saudi-fly-ash-based concrete. *Results Eng.* **2020**, *6*, 100118. [CrossRef]

54. Amran, M.; Fediuk, R.; Murali, G.; Avudaiappan, S.; Ozbakkaloglu, T.; Vatin, N.; Karelina, M.; Klyuev, S.; Gholampour, A. Fly ash-based eco-efficient concretes: A comprehensive review of the short-term properties. *Materials* **2021**, *14*, 4264. [CrossRef] [PubMed]

55. Siddika, A.; Amin, M.R.; Rayhan, M.A.; Islam, M.S.; Al Mamun, M.A.; Alyousef, R.; Mugahed Amran, Y.H. Performance of sustainable green concrete incorporated with fly ash, rice husk ash, and stone dust. *Acta Polytech.* **2021**, *61*, 279–291. [CrossRef]

56. Onaizi, A.M.; Lim, N.H.A.S.; Huseien, G.F.; Amran, M.; Ma, C.K. Effect of the addition of nano glass powder on the compressive strength of high volume fly ash modified concrete. *Mater. Today Proc.* **2021**, in press. [CrossRef]

57. Haruna, S.; Mohammed, B.S.; Wahab, M.M.A.; Kankia, M.U.; Amran, M.; Gora, A.M. Long-Term Strength Development of Fly Ash-Based One-Part Alkali-Activated Binders. *Materials* **2021**, *14*, 4160. [CrossRef]

58. Michałek, J.; Pachnicz, M.; Sobótka, M. Application of Nanoindentation and 2D and 3D Imaging to Characterise Selected Features of the Internal Microstructure of Spun Concrete. *Materials* **2019**, *12*, 1016. [CrossRef]

59. Michałek, J.; Sobótka, M. Assessment of Internal Structure of Spun Concrete Using Image Analysis and Physicochemical Methods. *Materials* **2020**, *13*, 3987. [CrossRef] [PubMed]

60. Dixon, D.E.; Abdun-nur, E.A.; Barton, S.G.; Bell, L.W.; Bias, S.J.; Carrasquillo, R.L.; Carrasquillo, P.M.; Carter, A.C.; Conrey, M.T.; Cook, J.E.; et al. Standard Practice for Selecting Proportions for Normal, Heavyweight, and Mass Concrete (ACI 211. 1-91) Reported by ACI Committee 211. *ACI Comm.* **2002**, *91*. Available online: https://www.academia.edu/38504100/ACI_211_1_91 _Standard_Practice_for_Selecting_Proportions_for_Normal_Heavyweight_and_Mass_Concrete (accessed on 20 November 2021).

61. ASTM C192 Standard Practice for Making and Curing Concrete Test Specimens in the Laboratory. *Am. Soc. Test. Mater.* **2016**, *4*, 1–8.

62. Neithalath, N.; Sumanasooriya, M.S.; Deo, O. Characterizing pore volume, sizes, and connectivity in pervious concretes for permeability prediction. *Mater. Charact.* **2010**, *61*, 802–813. [CrossRef]

63. Esmaeelnejad, L.; Siavashi, F.; Seyedmohammadi, J.; Shabanpour, M. The best mathematical models describing particle size distribution of soils. *Model. Earth Syst. Environ.* **2016**, *2*, 1–11. [CrossRef]

64. Shen, H.; Oppenheimer, S.M.; Dunand, D.C.; Brinson, L.C. Numerical modeling of pore size and distribution in foamed titanium. *Mech. Mater.* **2006**, *38*, 933–944. [CrossRef]

65. Eulitz, M.; Reiss, G. 3D reconstruction of SEM images by use of optical photogrammetry software. *J. Struct. Biol.* **2015**, *191*, 190–196. [CrossRef]

66. Hildenbrand-Habel, T.; Virnovsky, G.A.; Frette, O.I.; Fjelde, I. SEM imaging of dry and saturated porous rocks for modeling fluid distribution on pore scale. In Proceedings of the Society of Core Analyst's Symposium, Calgary, AB, Canada, 10–12 September 2007; pp. 1–6.

67. Haines, T.J.; Neilson, J.E.; Healy, D.; Michie, E.A.H.; Aplin, A.C. The impact of carbonate texture on the quantification of total porosity by image analysis. *Comput. Geosci.* **2015**, *85*, 112–125. [CrossRef]

68. Korte, D.; Kaukler, D.; Fanetti, M.; Cabrera, H.; Daubront, E.; Franko, M. Determination of petrophysical properties of sedimentary rocks by optical methods. *Sediment. Geol.* **2017**, *350*, 72–79. [CrossRef]

69. Onaizi, A.M.; Huseien, G.F.; Lim, N.H.A.S.; Amran, M.; Samadi, M. Effect of nanomaterials inclusion on sustainability of cement-based concretes: A comprehensive review. *Constr. Build. Mater.* **2021**, *306*, 124850. [CrossRef]

70. Loganina, V.; Sergeeva, K.; Fediuk, R.; Uvarov, V.; Vatin, N.; Vasilev, Y.; Amran, M.; Szelag, M. Increase the Performances of Lime Finishing Mixes Due to Modification with Calcium Silicate Hydrates. *Crystals* **2021**, *11*, 399. [CrossRef]

71. Lesovik, V.; Volodchenko, A.; Fediuk, R.; Mugahed Amran, Y.H.; Timokhin, R. Enhancing performances of clay masonry materials based on nanosize mine waste. *Constr. Build. Mater.* **2021**, *269*, 121333. [CrossRef]

72. Pandit, A.V.; Ranade, V.V. Chord length distribution to particle size distribution. *AIChE J.* **2016**, *62*, 4215–4228. [CrossRef]

73. Pleau, R.; Pigeon, M.; Laurencot, J.-L. Some findings on the usefulness of image analysis for determining the characteristics of the air-void system on hardened concrete. *Cem. Concr. Compos.* **2001**, *23*, 237–246. [CrossRef]

74. Pigeon, M.; Gagné, R.; Foy, C. Critical air-void spacing factors for low water-cement ratio concretes with and without condensed silica fume. *Cem. Concr. Res.* **1987**, *17*, 896–906. [CrossRef]

75. Łaźniewska-Piekarczyk, B. The influence of selected new generation admixtures on the workability, air-voids parameters and frost-resistance of self compacting concrete. *Constr. Build. Mater.* **2012**, *31*, 310–319. [CrossRef]

76. Powers, T.C.; Willis, T.F. *The Air Requirement of Frost-Resistant Concrete*; Portland Cement Association: Chicago, IL, USA, 1949.